ATP Converts $A\beta_{42}$ Oligomer into Off-pathway Species by Making Contact with Its Backbone Atoms Using Hydrophobic Adenosine

Ikuo Kurisaki[*1], Shigenori Tanaka[*1]

[1]Department of Computational Science, Graduate School of System Informatics, Kobe University, 1-1 Rokkodai-cho, Nada-ku, Kobe 657-8501, Japan

[*]Ikuo Kurisaki
E-mail: kurisaki@bear.kobe-u.ac.jp, Tel: +81-78-803-6472

[*]Shigenori Tanaka
E-mail: tanaka2@kobe-u.ac.jp, Tel: +81-78-803-6620

Abstract

Adenosine tri-phosphate (ATP) newly is expected to be involved in clearance of amyloid β 1–42 ($A\beta_{42}$) fibril and its precursors, $A\beta_{42}$ oligomer. Meanwhile the microscopic mechanism of the role in dissolving the protein aggregate still remains elusive. Aiming to elucidate the mechanism, we examined effects of ATP on the conformational change and thermodynamic stability of protomer dimer of $A\beta_{42}$ pentamer and tetramer, $A\beta_{42}(9)$, by employing all-atom molecular dynamics simulations. We observed interprotomer twisting and intraprotomer peeling of $A\beta_{42}(9)$. These conformational changes remarkably accelerate dissociation of the protomer dimer. However, the presence of ATP itself has no positive effect on dissociation processes of the protomer dimer and a monomer from the dimer, indicating its irrelevance to decomposition of $A\beta_{42}$ oligomer. Rather it could be supposed that ATP prevents additional binding and rebinding of $A\beta_{42}$ monomers to the $A\beta_{42}$ oligomer and it then converts $A\beta_{42}$ oligomer into off-pathway species which is excluded from $A\beta_{42}$ fibril growth processes. Interestingly hydrophobic adenosine in ATP makes contact with $A\beta_{42}(9)$ on their backbone atoms, with respect to both $A\beta_{42}$ monomers on the edge of $A\beta_{42}(9)$ and dissociated $A\beta_{42}$ monomers in $A\beta_{42}(9)$. These roles of ATP would be applied without regard to the structural polymorphism of $A\beta_{42}$ fibril.

Introduction

Fibril formation of amyloid β (1–42) ($A\beta_{42}$) peptide has been supposed to be the pathogenicity factor of Alzheimer disease.[1] To keep neuronal cells normal under physiological conditions, human cell intrinsically has some clearance mechanisms for those $A\beta_{42}$ conformers such as $A\beta_{42}$ fibrils, its precursors ($A\beta_{42}$ oligomer) referred to as *on-pathway* species, oligomeric assembly referred to as *off-pathway* species and the elementary components ($A\beta_{42}$ monomer and protomer) (Figure 1A and 1B).[2, 3] *On-pathway* species denote β-strand prone conformations similar to an oligomer in the fibril (*see* Figure 1A and 1B for example)[4], while *off-pathway* species, which are not competent for binding of additional $A\beta_{42}$ monomer, denote less- or non-β-strand prone conformation deviating from an oligomer in the fibril[5].

Adenosine tri-phosphate (ATP) currently is expected to be involved in the clearance of $A\beta_{42}$ fibrils. Hyman and his colleagues[6] clarified that ATP works as hydrotrope, a small molecule to solubilize hydrophobic molecules in aqueous solutions, by employing *in vitro* experiments. A more recent study by Haynes et al.[7] reported that this biological hydrotrope dissolves endogenous protein aggregates in *Xenopus* oocyte nucleoli. Surprisingly, ATP dissolved even thermodynamically stable protein aggregates such as preformed $A\beta_{42}$ fibril mixtures[6]. This newly discovered role of ATP now draws much

attention as an essential factor to control protein aggregates in the cell. Meanwhile the microscopic mechanism for ATP to dissolve the protein aggregate is not trivial and still remains elusive.

In order to elucidate the microscopic mechanism, it is indispensable to examine effects of ATP on the elementary processes of $A\beta_{42}$ fibril dissolution, $A\beta_{42}$ oligomer decomposition and its conversion into $A\beta_{42}$ conformers excluded from the fibril formation (Figure S1 in Supporting Information is an example to illustrate a set of the elementary processes). However, this investigation currently is challenging due to a molecular diversity of oligomers, protomers, and conformers not involved in the fibril formation[8]. A realistic reaction mechanism of $A\beta_{42}$ fibril formation is much more intricate than schematic illustrations of the process. It is therefore beyond abilities of current experimental techniques to selectively analyze the structure of a specific $A\beta_{42}$ oligomer to identify the essential steps where ATP functions in dissolving the protein aggregates.

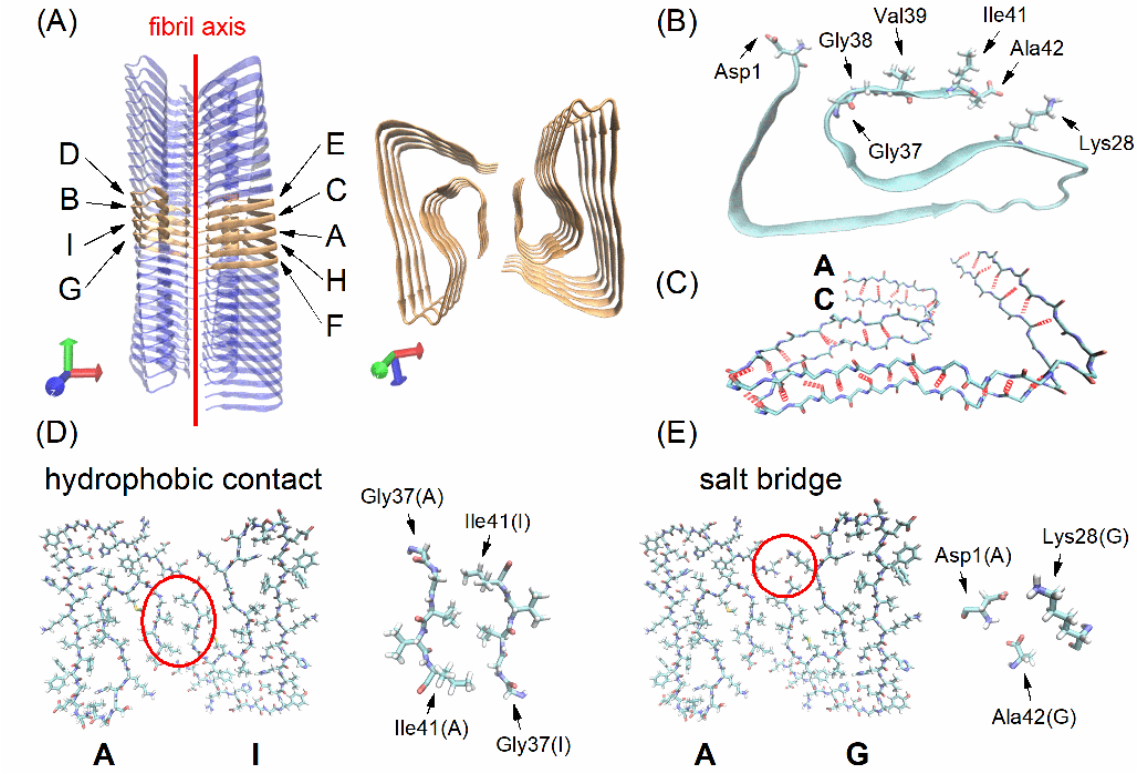

Figure 1. Structure of Aβ$_{42}$ oligomer. (A) Aβ$_{42}$ Oligomer; (B) Aβ$_{42}$ monomer conformation, referred to as LS shape; (C) Hydrogen bond formation between Aβ$_{42}$ monomers; (D) and (E) hydrophobic contact and salt bridge formation between protomers, respectively. A set of atomic coordination of Aβ$_{42}$ oligomer is derived from cryo-electron microscopy Aβ$_{42}$ structure (PDB entry: 5OQV). In panel (A), Aβ$_{42}$ nonamer, consisting of the two protomers (chains A, C, E, F and H; chains B, D, G and I), is highlighted by coloring orange. In panel (C), hydrogen bonds are shown by red dotted line. In panels (B), (D) and (E), amino acid residues involved in interprotomer interaction are emphasized on the right of the panel. Capital letters in panels denote chain IDs, which follow the original annotation given in the PDB information.

To overcome such technical difficulty, we here employ all-atom molecular dynamics simulations to specifically examine conformational change and thermodynamic stability of $A\beta_{42}$ nonamer, $A\beta_{42}(9)$ (highlighted by orange in Figure 1A)[9], a heterodimer of protomers consisting of $A\beta_{42}$ tetramer and pentamer (referred to as $A\beta_{42}(4)$ and $A\beta_{42}(5)$, respectively). $A\beta_{42}(9)$ is similar in size to the smallest $A\beta_{42}$ oligomer detected in aqueous solution[10]. We have supposed that the $A\beta_{42}(9)$ is one of minimal $A\beta_{42}$ on-pathway species and examining this model is practical to elucidate the microscopic mechanism of $A\beta_{42}$ fibril dissolution.

Since $A\beta_{42}$ fibril earns thermodynamic stability by non-bonded interaction (Figure 1C, 1D and 1E), $A\beta_{42}$ fibril formation is essentially a reversible process. It is thus supposed that clearance of $A\beta_{42}$ oligomers shifts equilibrium of $A\beta_{42}$ fibril formation toward that of $A\beta_{42}$ fibril dissolution. Recalling reversibility of $A\beta_{42}$ fibril formation, we presume two conjectures to understand a microscopic mechanism of $A\beta_{42}$ fibril dissolution by ATP: (1) ATP accelerates decomposition of $A\beta_{42}$ oligomers into elementary $A\beta_{42}$ fibril components, $A\beta_{42}$ protomer and $A\beta_{42}$ monomer; (2) ATP converts $A\beta_{42}$ oligomers into off-pathway species, which lack binding affinity to the $A\beta_{42}$ fibril axis ends, thus being excluded from $A\beta_{42}$ fibril growth processes.

We have then studied to verify our conjectures by considering the $A\beta_{42}$ nonamer, $A\beta_{42}(9)$ and we have obtained an evidence supporting the second conjecture, that ATP converts $A\beta_{42}$ oligomer into off-pathway species.

Materials and Methods

Setup of amyloid-β (1-42) nonamer systems

We used the cryo-electron microscopy (cryo-EM) structure for amyloid-β (1-42) nonamer (PDB entry: 5OQV[9]). Nε protonation state was employed for each of histidine residues, and all carboxyl groups in aspartate and glutamate residues were set to deprotonated state. Employing the $A\beta_{42}(9)$ structure, we prepared five $A\beta_{42}(9)$ systems, whose annotations and molecular components are summarized in Table 1. According to the study of Patel et al., $A\beta_{42}$ fibril is partly dissolved under physiological concentration of ATP-Mg^{2+} (8 mM). To discuss the effect of ATP-Mg^{2+} concentration, we examined five different conditions for ATP-Mg^{2+} concentration: 0, 8, 16, 32 and 64 mM. The detailed description for system setup is illustrated in Supporting Information (*see* **SI 1**).

Table 1. Molecular components of Aβ42 nonamer systems.

system	concentration of ATP-Mg^{2+} [mM]	number of molecule			
		ATP	Mg^{2+}	K^+	H_2O
No ATP-Mg^{2+}	0	0	0	27	30500
8 mM ATP-Mg^{2+}	8	5	5	37	30500
16 mM ATP-Mg^{2+}	16	10	10	47	30500
32 mM ATP-Mg^{2+}	32	20	20	67	30500
64 mM ATP-Mg^{2+}	64	40	40	107	30500

To calculate the forces acting among atoms, AMBER force field 14SB[11], TIP3P water model[12, 13], and JC ion parameters adjusted for the TIP3P water model[14, 15] were applied for amino acid residues, water molecules, and ions, respectively. Besides, the force field parameter sets developed by Meagher[16] and Bradbrook[17] were applied for adenosine tri-phosphate (ATP)[18] and Mg^{2+}, respectively. Molecular modeling of each Aβ42(9) system was performed using the LEaP modules in AmberTools 17 package[19].

Simulation setup

Molecular mechanics (MM) and molecular dynamics (MD) simulations were performed under the periodic boundary condition with GPU-version PMEMD module in AMBER 17 package[19] based on SPFP algorism[20] with NVIDIA GeForce GTX1080 Ti.

Electrostatic interaction was treated by the Particle Mesh Ewald method, where the real space cutoff was set to 9 Å. The vibrational motions associated with hydrogen atoms were frozen by SHAKE algorithm through MD simulations. The translational center-of-mass motion of the whole system was removed by every 500 steps to keep the whole system around the origin, avoiding an overflow of coordinate information from the MD trajectory format. These simulation conditions referred above were common in all of the simulations discussed in this manuscript.

Unbiased molecular dynamics simulation

Following temperature relaxation NVT simulations, tens of nanosecond NPT simulations (300 K, 1 bar) were performed and used for following analyses. The system temperature and pressure were regulated with Berendsen thermostat[21] with a 5-ps of coupling constant and Monte Carlo barostat with attempt of system volume change by every 100 steps, respectively. A set of initial atomic velocities was randomly assigned from the Maxwellian distribution at 0.001 K at the beginning of the NVT simulations. The time step of integration was set to 2 fs. The further details are shown in Supporting Information (*see* **SI 2**).

Steered and umbrella sampling molecular dynamics simulations

Dissociation processes of $A\beta_{42}$ monomer or $A\beta_{42}$ protomer were simulated by combining a steered molecular dynamics (SMD) simulation with umbrella sampling molecular dynamics (USMD) simulations. SMD was employed to dissociate an $A\beta_{42}$ monomer or protomer from the remaining part of $A\beta_{42}$(9). 0.25-ns SMD simulation was carried out under NPT condition (300 K, 1 bar), where the system temperature and pressure were regulated by Langevin thermostat with 1-ps^{-1} collision coefficient, and Monte Carlo barostat with attempt of system volume change by every 100 steps, respectively. The value of reaction coordinate was gradually changed through the SMD simulations by imposing the harmonic potential with the force constant of 100 kcal/mol/$Å^2$.

Then, certain numbers of snapshot structures were extracted from the SMD trajectory and employed for USMD windows. Following temperature relaxation simulations, several nanosecond NVT USMD simulations (300 K) were performed for each of the USMD windows (Tables S1 and S2 in Supporting Information for $A\beta_{42}$ protomer dissociation and $A\beta_{42}$ monomer dissociation, respectively). The system temperature was regulated using Langevin thermostat with 1-ps^{-1} collision coefficient. Each of the last 1-ns USMD trajectories was used to construct a potential of mean force. The reaction

coordinates chosen are discussed in Results and Discussion section. The further details are illustrated in Supporting Information (*see* **SI 3**).

Trajectory analyses

Interatomic distance, dihedral angle and root mean square deviation (RMSd) were calculated with the cpptraj module in AmberTools 17 package[19]. We calculated RMSd to the cryo-EM $A\beta_{42}$(9) structure[9] using the backbone heavy atoms (i.e., Cα, N, C and O). Besides, solvent accessible surface area (SASA) is calculated with NACCESS software [22]. We identify an atomic contact between an ATP molecule and an amino acid residue when the minimum interatomic distance between them was shorter than 4.0 Å. Salt bridge formation is identified when a distance between a nitrogen atom in a basic residue and an oxygen atom in an acidic residue is smaller than 3.2 Å.

Potential of mean force (PMF) was calculated with Weighed Histogram Analysis Method (WHAM)[23, 24] by using each set of USMD trajectories. Statistical errors of PMF values, $\sigma_{PMF}(\xi)$, were estimated by employing bootstrapped sampling[25]:

$$\sigma_{PMF}\left(\xi\right)=\left[\left(N_b-1\right)^{-1}\sum_{k=1}^{200}\left(W_{b,k}\left(\xi\right)-\left\langle W_b\left(\xi\right)\right\rangle\right)^2\right]^{\frac{1}{2}} \quad (1)$$

Here, N_b, ξ, and $W_{b,k}\left(\xi\right)$ denote the number of bootstrapped sampling, the reaction coordinate and the value of k^{th} bootstrapped potential of mean force at each point of

ξ, respectively. $\langle W_b(\xi)\rangle$ is average over all $W_{b,k}(\xi)$, where k ranges from 1 to 200.

Reaction rate, k_{TST}, is estimated by using Eyring's transition state theory:

$$k_{TST} = \frac{k_B T}{h} \exp\left(\frac{-\Delta F^{\dagger}}{k_B T}\right) \qquad (2)$$

Here, $\Delta F^{\dagger}$, h, k_B and T denote an activation barrier height, Planck constant, Boltzmann constant and a temperature of system, respectively. Reaction time scale, τ_{TST}, is defined as the inverse of k_{TST}. $\Delta F^{\dagger}$ is defined as $F(\xi_0') - F(\xi_0)$, where PMF has local minimum at ξ_0, and gradient of PMF turn from positive to negative values at ξ_0', which is greater than ξ_0.

Molecular structures were illustrated using Visual Molecular Dynamics (VMD).[26] A density distribution of ATP was calculated with the cpptraj module in AmberTools 17 package[19] and visualized using Volmap plugin of VMD[26]. Error bars are calculated from standard error and indicate 95% confidence interval if there is no annotation.

Results and Discussion

ATP makes contact with Aβ42 nonamer on its backbone atoms

We examined conformational fluctuation of Aβ42 nonamer, Aβ42(9), under thermal equilibrium by employing one hundred sets of 60-ns unbiased NPT MD simulations for each Aβ42(9) system. Figure 2A shows time-course change of averaged RMSd for Aβ42(9)

(RMSd analyses for each $A\beta_{42}$ monomer are discussed in Figure S2 in Supporting Information). For each of the five systems, it can be considered that the values reach equilibrium after 40 ns.

Meanwhile, the number of atomic contact between ATP and $A\beta_{42}(9)$ also reaches an equilibrium value after 40 ns (Figure 2B and 2C), for each of the four $A\beta_{42}(9)$-ATP-Mg^{2+} systems. The number of these contact increases with ATP concentration as expected. Considering the equilibrium of these two quantities, we employed partial MD trajectories in the period after 40 ns, and analyzed conformational properties of $A\beta_{42}(9)$ under thermal fluctuations.

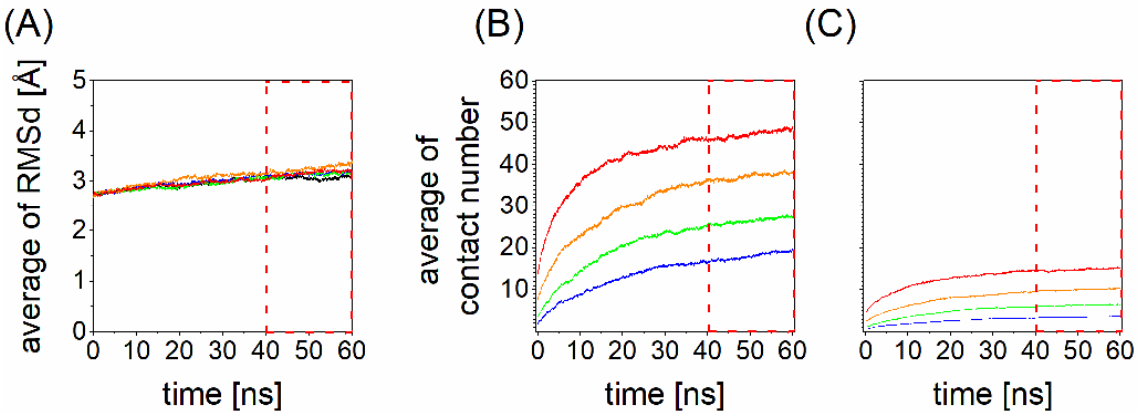

Figure 2. Time-course analyses of RMSd and atomic contact between ATP and Aβ$_{42}$ nonamer. (A) RMSd; (B) The number of amino acid residues making contact with ATP molecules; (C) The number of ATP molecules making contact with amino acid residues. Black line for No-ATP-Mg^{2+} system; blue line for 8 mM ATP-Mg^{2+} system; green line for 16 mM ATP-Mg^{2+} system; orange line for 32 mM ATP-Mg^{2+} system; red line for 64 mM ATP-Mg^{2+} system. Time domain assumed as convergence is indicated by the red dotted rectangle.

ATP contact with Aβ$_{42}$(9) implies functional similarity between ATP and morin. Morin is one of wine-related polyphenols and has potential to destabilize preformed Aβ$_{42}$ fibrils[27]. The earlier simulation study by Lenkul[28] proposed the atomistic mechanism for the role of morin in Aβ$_{42}$ fibril destabilization: it binds to the fibril axis ends of Aβ$_{42}$ oligomer and prevents an additional Aβ$_{42}$ monomer from binding to the oligomer. Recalling the role of morin in Aβ$_{42}$ oligomer, we then analyzed ATP contact on the

backbone atoms (N, C and O) for the Aβ$_{42}$ monomers at the fibril axis ends (chain D, E, F and G), employing the one hundred 60-ns unbiased NPT MD simulations for 64 mM ATP-Mg^{2+} system as representative. Concentration of 64 mM is c.a. 10-fold greater than that under physiological condition. The concentration of Aβ$_{42}$ monomer in the simulation box is c.a. 1 mM, while experimental Aβ$_{42}$ monomer concentration is up to 0.1 mM[29]. Then, we employed this system considering that our simulation condition is similar to experiment condition in the ratio between ATP and Aβ$_{42}$ monomers.

Table 2 summarizes the number of atomic contact between ATP and Aβ$_{42}$ monomers at the fibril axis ends, the chains D, E, F and G shown in Figure 1A (time-course analyses of the atomic contact are discussed in Figures S3 and S4) and the remaining five monomers located at the middle of the protomers, the chains A, B, C, H and I. For each of panels, we assumed convergence of the value after 40 ns. 1.8 or more residues in each of the four Aβ$_{42}$ monomers make contact with ATP on their backbone atoms, while c.a. one ATP is involved in contact with backbone atoms of each of the monomers. Since ATP partially covers the fibril axis ends, it could have potential to prevent additional monomer binding to the fibril axis end of Aβ$_{42}$ oligomers as well as morin.

The number of atomic contact between ATP and Aβ$_{42}$ monomers at the fibril axis ends are greater than that at the middle of the protomers. Nonetheless ATP could not

preferentially make contact with Aβ42(9) backbone atoms at the fibril axis end. The middle part of Table 2 shows the SASA-normalized number of amino acid residue contact with ATP. These values are not necessarily higher in the monomers at the fibril ends. This observation suggests non-site-specific interaction between ATP and Aβ42(9).

Taken together, the observations for ATP contacts at the fibril axis end could support our second conjecture in the point that Aβ42 oligomers are excluded from the fibril growth process by ATP contact.

Table 2. Atomic contact between ATP and backbone atoms of Aβ42 monomer at the fibril axis end for 64 mM ATP-$Mg2^{+}$ system.

part of ATP	chain ID*								
	A	B	C	**D**	**E**	**F**	**G**	H	I
	amino acid residue contact with ATP								
ATP	0.5 ± 0.1	0.9 ± 0.2	0.7 ± 0.2	2.7 ± 0.6	2.7 ± 0.6	1.9 ± 0.4	2.5 ± 0.4	0.8 ± 0.2	1.1 ± 0.3
adenosine	0.4 ± 0.1	0.9 ± 0.2	0.6 ± 0.2	2.6 ± 0.5	2.6 ± 0.6	1.8 ± 0.4	2.3 ± 0.4	0.6 ± 0.2	1.0 ± 0.3
tri-phosphate	0.0 ± 0.0	0.0 ± 0.0	0.0 ± 0.0	0.1 ± 0.0	0.2 ± 0.1	0.3 ± 0.1	0.3 ± 0.1	0.2 ± 0.1	0.1 ± 0.1
	amino acid residue contact with ATP (normalized with SASA** and multiplied by 10^3)								
ATP	2.2 ± 0.6	4.0 ± 0.9	2.9 ± 0.8	3.1 ± 0.6	3.0 ± 0.7	2.4 ± 0.5	3.1 ± 0.5	3.0 ± 0.8	4.3 ± 1.0
adenosine	2.0 ± 0.6	3.8 ± 0.9	2.7 ± 0.8	3.0 ± 0.6	2.9 ± 0.7	2.2 ± 0.5	2.9 ± 0.5	2.5 ± 0.7	4.0 ± 1.0
tri-phosphate	0.2 ± 0.1	0.1 ± 0.1	0.2 ± 0.1	0.1 ± 0.0	0.2 ± 0.1	0.4 ± 0.1	0.3 ± 0.1	0.6 ± 0.3	0.4 ± 0.2
	ATP contact with amino acid residues								
ATP	0.3 ± 0.1	0.6 ± 0.1	0.5 ± 0.1	1.3 ± 0.2	1.2 ± 0.2	1.1 ± 0.2	1.3 ± 0.2	0.5 ± 0.1	0.7 ± 0.2
adenosine	0.3 ± 0.1	0.6 ± 0.1	0.4 ± 0.1	1.2 ± 0.2	1.1 ± 0.2	1.0 ± 0.2	1.2 ± 0.2	0.4 ± 0.1	0.6 ± 0.1
tri-phosphate	0.0 ± 0.0	0.0 ± 0.0	0.0 ± 0.0	0.1 ± 0.0	0.2 ± 0.0	0.3 ± 0.1	0.2 ± 0.1	0.1 ± 0.1	0.1 ± 0.1

*Chain IDs follow the original annotation given in the PDB information for Aβ42 structure

by cryo-electron microscopy (PDB entry: 5OQV) and Aβ42 monomer chain at the fibril axis end is highlighted by boldface.

**SASA denotes solvent accessible surface area [Å^2] and are calculated for main chain atoms (Cα, C, N, O and H) in each monomer.

It should be noted that ATP contact with these backbone atoms is mostly due to the hydrophobic adenosine (Table 2). Amino group and hydroxyl groups in adenosine play significant roles in stable contact with Aβ42 monomer on their backbone. This issue also will be addressed with regard to an Aβ42 monomer dissociation process in the later part of this section.

Aβ42 nonamer shows interprotomer twisting and intraprotomer peeling under thermal fluctuation

In order to analyze conformational fluctuation of Aβ42(9) in atomistic details, we defined three structure descriptors typical of Aβ42(9), the interprotomer twisting angle (θ_T), the intraprotomer peeling distances (d_P^4 and d_P^5) and the interprotomer center of gravity distance (d^{4-5}), which are explained in Figure 3A, 3B and 3C, respectively. The superscripts '4' and '5' denote Aβ42(4) and Aβ42(5), respectively. They were calculated for each of all the snapshots structures.

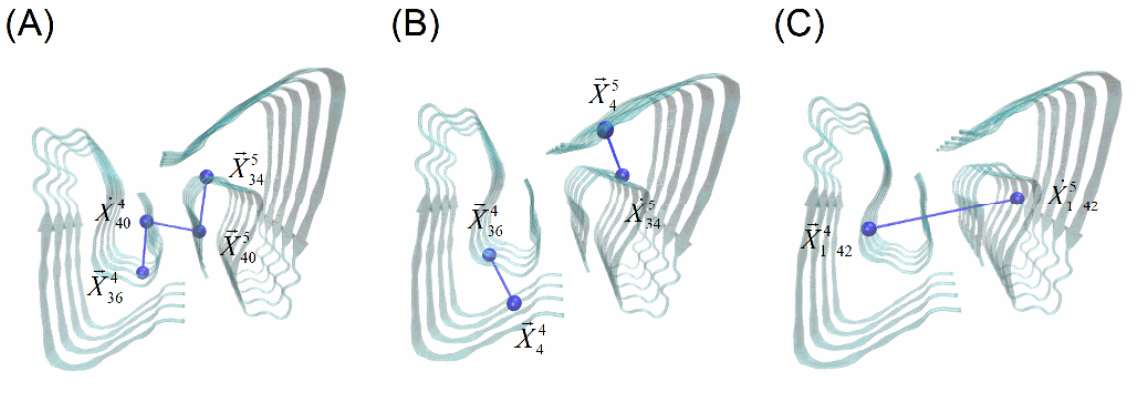

Figure 3. Schematic illustration for the structural descriptors of Aβ$_{42}$ nonamer. (A) interprotomer twisting angle; (B) intraprotomer peeling distances; (C) interprotomer center of gravity distance. $\vec{X}^m_n$ denotes center of gravity, which is calculated for the *m* C_α atoms of the n^{th} residues in the *m* mer protomer in the Aβ$_{42}$ nonamer. A blue ball represents center of gravity.

Table 3 gives averaged values of the structure descriptors calculated for each of the five systems, and also those for the cryo-EM structure[9] as the reference. Each of the systems shows remarkable difference in twisting angle, compared with the cryo-EM structure. Meanwhile, both the values of peeling distances and those of interprotomer center of gravity distance are similar between the cryo-EM structure and each of the systems.

Table 3. Statistical analyses of structure descriptors and number of interprotomer salt bridge formation

system	twisting angle [deg.]	peeling distance [Å]		center of gravity distance [Å]	number of salt bridge formation
		4 mer	5 mer		
Reference †	174.4	11.5	11.5	30.3	8
No ATP-Mg^{2+}	197.3 ± 9.4*	12.1 ± 2.2	12.3 ± 1.5	32.5 ± 0.5	16.4 ± 0.8
8 mM ATP-Mg^{2+}	197.4 ± 10.6	12.3 ± 2.7	12.4 ± 1.6	32.5 ± 0.5	16.3 ± 0.8
16 mM ATP-Mg^{2+}	197.3 ± 9.5	12.2 ± 2.6	12.4 ± 1.6	32.5 ± 0.6	15.7 ± 0.8
32 mM ATP-Mg^{2+}	197.9 ± 11.2	12.0 ± 2.4	12.5 ± 1.8	32.5 ± 0.5	15.4 ± 0.8
64 mM ATP-Mg^{2+}	198.3 ± 11.2	12.1 ± 2.0	12.5 ± 1.8	32.5 ± 0.5	14.5 ± 0.8

†$A\beta_{42}$ nonamer resolved by cryo-electron microscopy (PDB entry: 5OQV).

*Error indicates 95% confidential interval, where error value is estimated from standard deviation.

The remarkable change for the twisting angle could be explained by absence of atomic contact of $A\beta_{42}(9)$ with remaining part of $A\beta_{42}$ amyloid fibril (see Figure 1A, the left illustration). Under the experimental condition, each $A\beta_{42}$ monomer on the edge of protomer (Chains D, E, G or F) makes atomic contact with the neighboring monomer which is not provided in the PDB's atomic coordinate file (*see* Figure 1A, the left illustration). Meanwhile, $A\beta_{42}(9)$ in our simulation has no atomic contact with any other $A\beta_{42}$ monomers (*see* Figure 1A, the right illustration). Loss of atomic contact with

neighboring monomer possibly makes the two protomers reorient to earn energetic stabilization as $A\beta_{42}(9)$ in aqueous solution. This observation is supported by the increased number of salt bridge between the protomers. (Table 3).

According to the analyses discussed above, we found conformational fluctuation of $A\beta_{42}(9)$ with regard to the twisting angle and peeling distances within a period of tens of nanoseconds. Meanwhile, in terms of these structure descriptors, each conformational characteristic of $A\beta_{42}(9)$ under thermal fluctuation is similar among the five systems (*see* Table 3) so that we could say that it is an intrinsic property of $A\beta_{42}(9)$ with no regard to the presence of ATP molecules.

To precisely examine influence of twisting and peeling in the following $A\beta_{42}(9)$ dissociation simulation, the MD simulation-derived snapshot structures were classified into 12 groups, by employing the twisting angle (θ_T) and the two peeling distances (d_P^4 and d_P^5) as classification parameters.

We use the following symbols (−, +, R and L) in classification of $A\beta_{42}(9)$ conformation. Minus sign (−) means that a structural descriptor has a value close to the averaged one: the value fall within range of the average value $\pm 2 \times$ S.D. Meanwhile the other three signs denote that a structural descriptor has values away from the averaged one: the value is found out of range of the average value $\pm 2 \times$ S.D. Cross (+) is for peeling in $A\beta_{42}(4)$

and that in $A\beta_{42}(5)$. 'R' and 'L' are for the deviation in counterclockwise and clockwise directions with regard to twisting angle, respectively.

A class is defined as combination of three letters: the first, second and third letters are for twisting, peeling of $A\beta_{42}(5)$ and peeling of $A\beta_{42}(4)$. For example, R−+ is assigned to a conformation which shows counterclockwise twisting and peeling of $A\beta_{42}(4)$. Occupancies of classes are given in Tables S3-7 in Supporting Information, for each of the $A\beta_{42}(9)$ systems, indicating negligible effects of ATP on repertoire of $A\beta_{42}(9)$ conformations.

Among the twelve classes, the four (−−−, −++, L−−, R−−) occupy c.a. 90 % of snapshot structures for each of the five systems. Besides, these four classes contain an average conformation (−−−) and typical ones which show significant deviations of intraprotomer peeling, interprotomer clockwise twisting and interprotomer counterclockwise twisting (−++, L−− and R−−, respectively). We here thus supposed that considering the four classes is enough to examine the influence of conformational change of $A\beta_{42}(9)$ on dissociation processes.

We defined a representative structure for each of the four class by using the score function:

$$Score\left(\theta_T, d_P^4, d_P^5\right) = \frac{\left|\theta_T - \theta_{T,Ave}\right|}{\theta_{T,SD}} + \frac{\left|d_P^4 - d_{P,Ave}^4\right|}{d_{P,SD}^4} + \frac{\left|d_P^5 - d_{P,Ave}^5\right|}{d_{P,SD}^5} \qquad (3)$$

We considered this function to evaluate structural deviation of an MD-derived Aβ42(9) conformation from the averaged one of the corresponding ATP-Mg^{2+} system. As addressed above, the twisting angle, peeling distances of Aβ42(4) and Aβ42(5) are denoted by θ_T, d_P^4 and d_P^5. Subscripts *Ave* and *SD* mean average and standard deviation, respectively (specific values for each ATP-Mg^{2+} system are shown in Table 3). The representative structure of −−− and those of the other three correspond to the smallest and largest values of the score function, respectively. The former is supposed to take an average structure, while each of the latter three is supposed to take a structure with relatively large deviation with regard to these structure descriptors.

These four representative structures were employed for the following dissociation simulations of Aβ42(9) (Figure 4A-D, and Table 4). They were derived from 64 mM ATP-Mg^{2+} system. This is because values of twisting angle and peeling distances are relatively large compared with the other four systems (*see* Tables S3-7 in Supporting Information), which are expected to lead to apparent effects of conformational difference from −−− on dissociation processes.

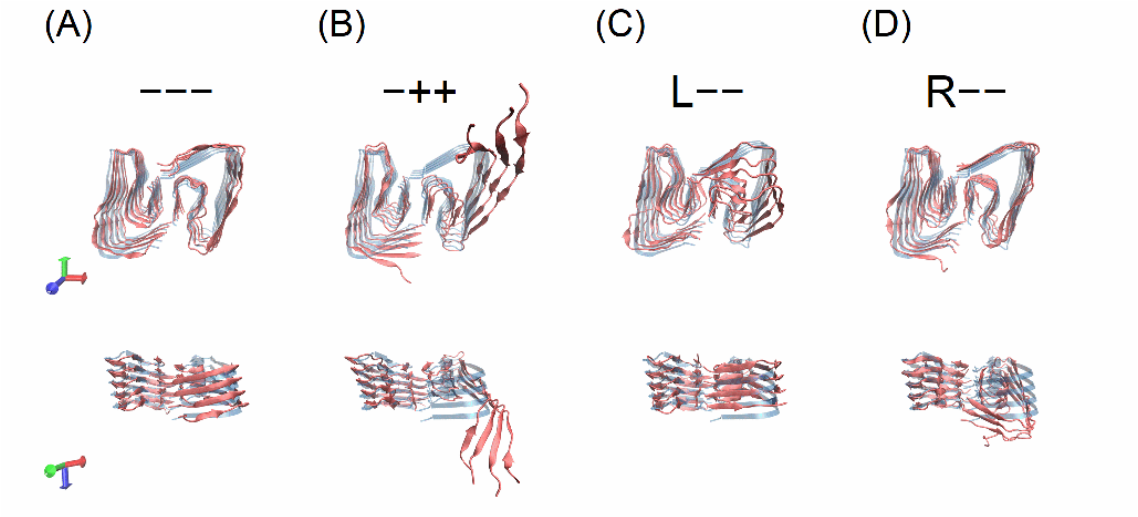

Figure 4. Representative conformations of $A\beta_{42}$ nonamer in aqueous solution. A conformation annotation is given on the top of each panel. (A) Standard conformation (−−−); (B) Peeling on both protomer (−++); (C) Twisting toward left side (L−−); (D) Twisting toward right side (R−−). The cryo-electron microscopy $A\beta_{42}$ nonamer structure (PDB entry: 5OQV), colored in transparent blue, is superposed on each representative conformation.

Table 4. Values of the structural descriptors and number of interprotomer salt bridge formation for the four representative conformations

conformation †	twisting angle [deg.]	peeling distance [Å]		center of gravity distance [Å]	number of interprotomer salt bridge
		4 mer	5 mer		
− − −	198.3	12.1	12.5	31.8	24
−++	191.8	17.6	32.2	35.7	11
L− −	183.9	13.9	9.2	31.7	17
R− −	255.9	11.3	14.1	32.3	16

†−−− for standard conformation; −++ for peeling on both protomer conformation; L−− for twisting toward left side conformation; R−− for twisting toward right side conformation.

Protomer dissociation proceeds through conformational change

We discuss effects of ATP on $A\beta_{42}(9)$ decomposition by considering $A\beta_{42}(9)$ protomer and monomer dissociation processes through the remaining parts of this section. We here address the former, $A\beta_{42}(9)$ protomer dissociation process. No ATP-Mg^{2+} and 64 mM ATP-Mg^{2+} systems were reconstructed with the four representative conformations and examined hereafter (the details are given in **SI 3** in Supporting Information). Here the 64 mM ATP-Mg^{2+} condition was chosen, expecting that the effect of ATP on $A\beta_{42}(9)$ is

emphasized by enhancing Aβ42(9)-ATP interaction more than in the system under physiological condition.

We first considered No ATP-Mg^{2+} system. Aβ42(9) protomer dissociation process is simulated by a steered MD (SMD) method, where the interprotomer center of gravity distance (d_{4-5}) is employed as the reaction coordinates (*see* Figure 3C) and steered to increase by 60 Å in each SMD simulation. We observed that each of the protomers dissociates without apparent structural deviations, except for −++ for the No ATP-Mg^{2+} system (*see* Figure S5 in Supporting Information). The structural deviation for −++ is explained by the fluctuation of peeling distances, although the distances still satisfy the criteria of −++ (*see* Figure S6 in Supporting Information). We then suppose that structural deviation observed in the SMD simulations for −++ are essentially irrelevant for the following analyses. This observation similarly holds for the 40 mM ATP-Mg^{2+} system, so that we here address it in advance (*see* Figures S6 and S7 in Supporting Information).

As shown in Figure 5A-D, each of the PMFs has one activation barrier toward the dissociation direction, appearing to be up-hill. The PMF for −++ is different from those for the other three in the position of minimum. This is simply because a positions of center of mass of −++ is shifted due to peeling. This difference changes appearance of the PMF subtly but is not essential in the following discussion.

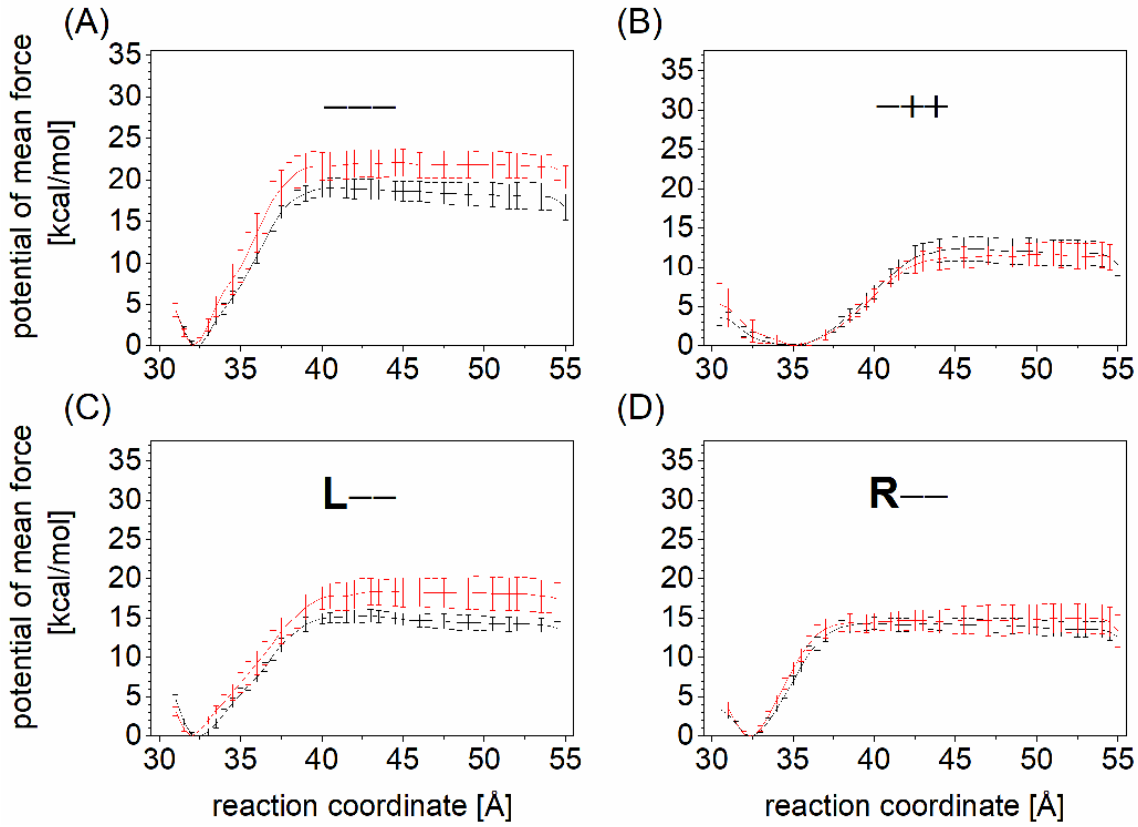

Figure 5. Potential of mean force of Aβ42 protomer dissociation for No ATP-Mg^{2+} and 64 mM ATP-Mg^{2+} systems. (A) Standard conformation (———); (B) Peeling on both protomer conformation (—++); (C) Twisting toward left side conformation (L——); (D) Twisting toward right side conformation (R——). A conformation annotation is given on the top of each panel. Error bar indicates 95% confidential interval. Black lines for No ATP-Mg^{2+} system; red lines for 64 mM ATP-Mg^{2+} system.

The PMF for ——— shows the highest activation barrier, 19.1 kcal/mol of the four systems. Meanwhile those for —++, L—— and R—— are 12.4, 15.3 and 14.3 kcal/mol,

respectively. It can be supposed that $A\beta_{42}(9)$ conformational changes from −−− accelerate protomer dissociation reaction with lower activation barrier. This could be due to weakening interprotomer interaction, which acts between N-terminal of one protomer and C-terminal of the other (*see* Figure 1E). Actually, we can find apparent reduction of salt bridge formation between the protomer in −++, L−− and R−−, compared with −−−. The number of interprotomer salt bridges is 24 as for −−−, while it is reduced to 17 or lesser with regard to the remaining three (Table 4).

According to the heights of activation barriers calculated above, the time scale of protomer dissociation approximately ranges from milliseconds to tens of second (Table 5). This time scale is greater than that of relaxation of ATP contact with $A\beta_{42}(9)$, tens of nanoseconds (*see* Figure 2B and 2C). Under such a circumstance, ATP contact with $A\beta_{42}(9)$ probably is relaxed in advance of $A\beta_{42}$ protomer dissociation.

Table 5. Physicochemical characterization of potential of mean force of $A\beta_{42}$ protomer dissociation for No ATP-Mg^{2+} and 64 mM ATP-Mg^{2+} systems. Free energy barrier, reaction rate calculated with Eyring's transition theory and reaction time are denoted by $\Delta F^{\ddagger}$, k_{TST} and τ_{TST} (inverse of k_{TST}), respectively.

conformation	No ATP-Mg^{2+}			64 mM ATP-Mg^{2+}		
	$\Delta F^{\ddagger}$ [kcal/mol]	k_{TST} [s^{-1}]	τ_{TST} [s]	$\Delta F^{\ddagger}$ [kcal/mol]	k_{TST} [s^{-1}]	τ_{TST} [s]
− − −	19.1 (1.2)	7.2E-02	1.4E+01	21.7 (1.8)	1.0E-03	9.7E+02
−++	12.4 (1.5)	5.5E+03	1.8E-04	11.4 (1.4)	3.2E+04	3.1E-05
L− −	15.3 (0.8)	4.4E+01	2.3E-02	17.8 (1.6)	6.8E-01	1.5E+00
R− −	14.3 (0.9)	2.5E+02	4.0E-03	14.1 (1.8)	3.4E+02	2.9E-03

†−−− for standard conformation; −++ for peeling on both protomer conformation; L−− for twisting toward left side conformation; R−− for twisting toward right side conformation.

*Value inside parentheses denotes 95% confidential interval.

Considering these two molecular events different in the time scale, we simulated protomer dissociation after relaxation of ATP contact with $A\beta_{42}(9)$ (Figure 6) (*see* **SI 3** in Supporting Information for computational details) and calculated the PMFs of 64 mM ATP-Mg^{2+} system (Figure 5A-D). The height of an activation barrier is reduced by conformational change from −−−, being similar to the cases of the No ATP-Mg^{2+} systems

(Table 5). Meanwhile, we cannot find significant difference in height of activation barrier between PMFs in the absence of ATP and that in the presence of ATP. The timescale of protomer dissociation still is between milliseconds and tens of second.

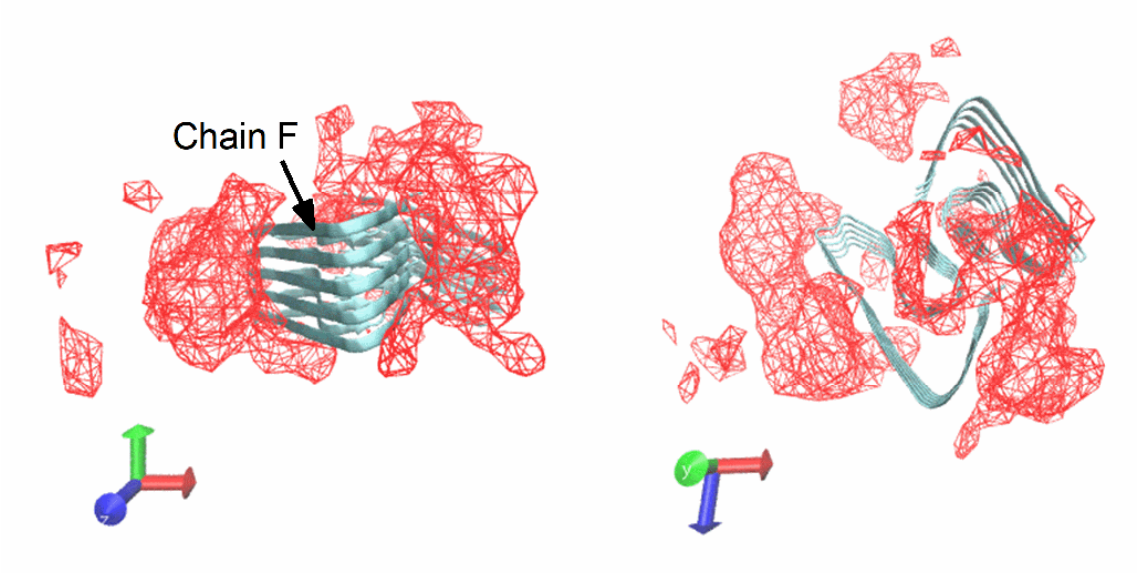

Figure 6. Spatial distribution of ATPs around $A\beta_{42}$ nonamer under 64 mM ATP-Mg^{2+} condition. Locations with density > 0.0075 $Å^{-3}$ is drawn with red wire frame.

These PMF analyses indicate that ATP has no remarkable influence on $A\beta_{42}(9)$ protomer dissociation reaction, so that we could not obtain evidences supporting our first conjecture. Nonetheless, physicochemical insights derived from the PMF analyses still are worth discussing in the context of thermodynamic stability of $A\beta_{42}(9)$ oligomer. Recalling the heights of activation barriers, the time scale of $A\beta_{42}(9)$ protomer

dissociation approximately ranges from milliseconds to tens of second (Table 5), and then is similar to those of protein-protein dissociation processes previously reported[30-32]. Considering that Zhang and colleagues[33] reported that a protein complex dissociation undergoes rotational motion in the initial step, it could be said that $A\beta_{42}(9)$ should assume R−− or L— at the beginning of protomer dissociation process under thermal fluctuation. According to these observations, $A\beta_{42}(9)$ as $A\beta_{42}(5)$-$A\beta_{42}(4)$ complex possibly is similar to biologically functional protein-protein complexes in thermodynamic stability.

Meanwhile, more elongated $A\beta_{42}$ oligomers possibly show greater thermodynamic stability. It is presumed that elongation of $A\beta_{42}$ oligomer accompanies enthalpy gain and entropy loss to earn thermodynamic stability. It would result in restriction of configurations of the protomers, then suppressing the rotational motion between a pair of protomers as represented by R−− and L−−. Suppressing such structural changes would practically keep an activation barrier of the protomer dissociation higher. This observation seems to be worth studying to obtain deeper insights into a microscopic mechanism of $A\beta_{42}$ fibril formation process, although it is beyond the scope of this study. We then leave it as the future problem.

ATPs make contact with partially dissociated $A\beta_{42}$ monomer and

convert Aβ42 oligomer into off-pathway species

Next, we examined the effect of ATP on Aβ42 monomer dissociation. In Aβ42 monomer dissociation SMD simulations, the distance between center of gravity of the monomer in Aβ42(5) (Chain F, referred to as Aβ42(F) hereafter) and that of the remaining part of the pentamer (Chains A, C, E and H, referred to as Aβ42(ACEH)) is employed as the reaction coordinate (Figure 7). A value of the reaction coordinate was steered to increase by 40 Å in each SMD simulation.

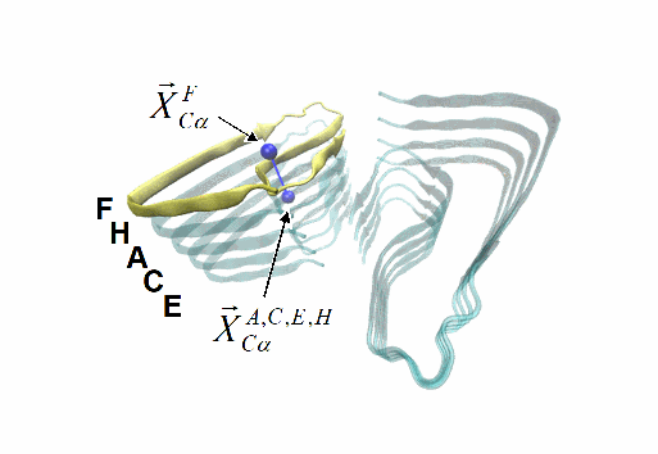

Figure 7. Schematic illustration of reaction coordinate for monomer dissociation simulation. $\vec{X}^{m}_{n}$ denotes center of gravity, which is calculated for the Cα atoms of a set of Aβ42 monomer chain, *m*. The monomer undergoing dissociation is distinguished by coloring yellow. Bold capital letters beside Aβ42 pentamer denote chain ID, which follows original annotation given in PDB information of cryo-electron microscopy Aβ42 structure

(PDB entry: 5OQV). Blue balls represent center of gravity for each descriptor.

The dissociated $A\beta_{42}$(F) shows a partially or fully unfolded conformation (Figure 8). We suppose that it could reflect structural properties of $A\beta_{42}$ monomer under $A\beta_{42}$ oligomer formation condition. Each $A\beta_{42}$ monomer in an oligomer assumes thermodynamically unstable LS shape conformation (*see* Figure 1B). Actually, this conformation has no α-helices and no intramolecular β-sheets so that it earns energetic stability by forming hydrogen bonds with neighboring $A\beta_{42}$ monomers (*see* Figure 1C). It is then supposed that $A\beta_{42}$ monomer folding into the LS shape conformation is coupled with its binding to $A\beta_{42}$ oligomer and its reverse reaction, $A\beta_{42}$ monomer dissociation, is coupled with unfolding of LS shape conformation.

We first analyzed the PMFs of $A\beta_{42}$(9) monomer dissociation in absence of ATP-Mg^{2+} (Figure 9A-D). The PMFs for −−− and R−− are different from those for −++ and L−− with respect to concerning the steep slopes from the minima. Nonetheless, these PMFs are similar in their physicochemical characters. They have no intermediate states and thus essentially have each one activation barriers toward the dissociation direction, appearing to be up-hill with no regard to conformations of $A\beta_{42}$(9).

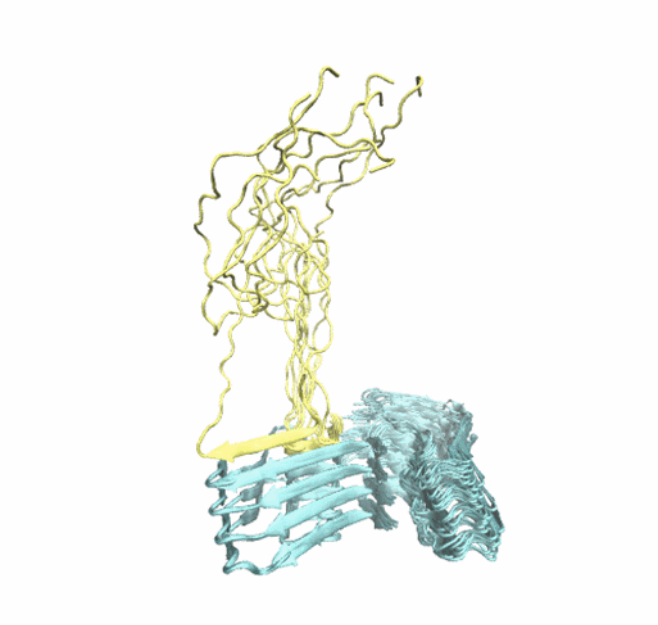

Figure 8. Ensemble of snapshot structures of monomer dissociated $A\beta_{42}$ nonamer, obtained from independent twelve steered MD simulation for No ATP-Mg^{2+} system of standard conformation (−−−), which is similar to cyro-EM structure (PDB entry: 5OQV). The monomer undergoing dissociation is distinguished by coloring yellow.

According to the heights of activation barriers calculated above, the time scale of $A\beta_{42}$ monomer dissociation approximately ranges from sub-microseconds to milliseconds (Table 6), thus being greater than that of relaxation of ATP contact on $A\beta_{42}(9)$ (*see* Figure 2B and 2C). We then have performed $A\beta_{42}$ monomer dissociation simulations under the condition that ATP contact with $A\beta_{42}(9)$ has been relaxed (*see* Figure 6), as is the case of the protomer dissociation simulations. Interestingly, addition of ATP suppresses $A\beta_{42}$

monomer dissociation. Each of the PMFs for 64 mM ATP-Mg^{2+} system has the activation barrier whose height is larger than 18.2 kcal/mol (Figure 9A-D). According to the heights of the activation barriers, the time scale of monomer dissociation is in range of seconds or longer (Table 6).

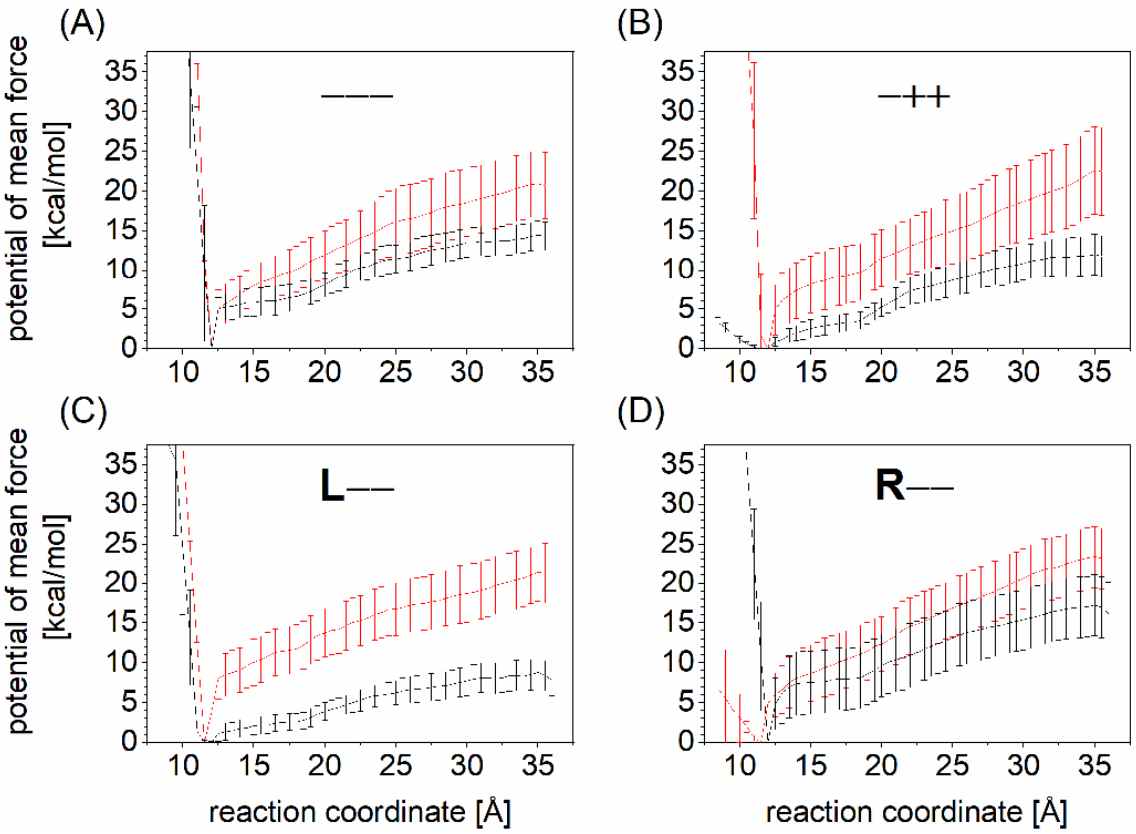

Figure 9. Potential of mean force of $A\beta_{42}$ monomer dissociation for No ATP-Mg^{2+} and 64 mM ATP-Mg^{2+} systems. (A) Standard conformation (———); (B) Peeling on both protomer conformation (–++); (C) Twist toward left side conformation (L––); (D) Twist

toward right side conformation (R−−). Error bar indicates 95% confidence interval. Black lines for No ATP-Mg^{2+} system; red lines for 64 mM ATP-Mg^{2+} system.

Table 6. Physicochemical characterization of potential of mean force of $A\beta_{42}$ monomer dissociation for No ATP-Mg^{2+} and 64 mM ATP-Mg^{2+} systems. Free energy barrier, reaction rate calculated with Eyring's transition theory and reaction time are denoted by $\Delta F^{\ddagger}$, k_{TST} and τ_{TST} (inverse of k_{TST}), respectively.

conformation	No ATP-Mg^{2+}			64 mM ATP-Mg^{2+}		
	$\Delta F^{\ddagger}$ [kcal/mol]	k_{TST} [s^{-1}]	τ_{TST} [s]	$\Delta F^{\ddagger}$ [kcal/mol]	k_{TST} [s^{-1}]	τ_{TST} [s]
−−−	13.7 (1.8)	6.9E+02	1.5E-03	21.0 (4.2)	3.6E-03	2.8E+02
−++	11.6 (2.3)	2.1E+04	4.8E-05	23.2 (3.5)	7.0E-05	1.4E+04
L−−	8.1 (1.8)	7.4E+06	1.3E-07	18.2 (5.3)	3.6E-01	2.8E+00
R−−	17.2 (3.8)	1.8E+00	5.4E-01	22.6 (5.5)	2.1E-04	4.8E+03

†−−− for standard conformation; −++ for peeling on both protomer conformation; L−− for twisting toward left side conformation; R−− for twisting toward right side conformation.

*Value inside parentheses denotes 95% confidence interval.

In contrary to our first conjecture, ATP rather suppresses $A\beta_{42}$ monomer dissociation. It can thus be supposed that $A\beta_{42}$ fibril dissolution under the presence of ATP is due to

molecular processes except for acceleration of $A\beta_{42}$ oligomer decomposition. On the other hand, there still is room to consider our second conjecture, because our analyses showed the capability of ATP to exclude $A\beta_{42}$ monomers from the $A\beta_{42}$ fibril formation process (*see* Table 2 and the related discussion). We then examine the effects of ATP on $A\beta_{42}$(F) under dissociation conditions by keeping our second conjecture in mind in the following.

Suppression of $A\beta_{42}$(F) dissociation observed above possibly is due to ATP contact with $A\beta_{42}$(F). As addressed above, there are a certain amount of ATPs making stable contact with $A\beta_{42}$(9) (*see* Figure 2B and 2C, and Figure 6). A part of such ATPs could interfere with $A\beta_{42}$(F) dissociation by anchoring the monomer around the oligomer. We then speculate the presence of ATP which makes steady contact with both $A\beta_{42}$(F) and the remaining of the $A\beta_{42}$(9).

Meanwhile, it is possible to consider the effect of ATP on exclusion of dissociated $A\beta_{42}$ monomers from $A\beta_{42}$ oligomer formation process. Assuming ATP contact with dissociated $A\beta_{42}$ monomer on the backbone atoms (N, C and O), such a contact competes with intermonomer hydrogen bond formation and refolding to LS shape conformation (*see* Figure 1B and 1C) to interfere with rebinding of the dissociated monomer to the $A\beta_{42}$ oligomer. The above assumption seems physicochemically reasonable because we already observed that ATP makes contact with $A\beta_{42}$ monomers at the fibril axis ends on

their backbone atoms. ATP could make contact with (partially) unfolded $A\beta_{42}$(F) similarly. We then made a speculation that ATP stably makes contact with $A\beta_{42}$(F) on the backbone atoms.

To verify the speculation, we performed fifty unbiased 40-ns NPT MD simulations starting from $A\beta_{42}$(9) with (partially) dissociated $A\beta_{42}$(F) and analyzed ATP contact on the monomer. Recalling the similarity in physicochemical characteristics of $A\beta_{42}$ monomer dissociation PMF among the four $A\beta_{42}$(9) 64 mM ATP-Mg^{2+} systems (*see* Figure 9A-D), we considered the standard $A\beta_{42}$(9) system (−−−) as representative.

We classified ATPs making contact with $A\beta_{42}$(F) with three types: ATPs making contact with the remaining part of the $A\beta_{42}$ oligomer simultaneously (ATP^S; Figure 10A); ATPs making contact with other ATPs forming cluster with the remaining of $A\beta_{42}$(9) (ATP^C; Figure 10B); ATPs making no contact with the $A\beta_{42}$ monomers except for $A\beta_{42}$(F) (ATP^F; Figure 10C). Calculating the number of each of ATP types along time-course, we observed convergence after 20 ns so that we analyzed the values for the time domain between 20 and 40 ns (*see* Figure S8 in Supporting Information). The numbers of ATP^S and ATP^C are 1.6 ± 0.3 and 1.8 ± 0.5, respectively. Meanwhile, the number of ATP^F is 0.6 ± 0.3. The analyses for ATP making contact with $A\beta_{42}$(F) thus indicate that a certain amount of ATP makes contact with $A\beta_{42}$(F) and the remaining of the $A\beta_{42}$(9). These ATPs

would anchor $A\beta_{42}$(F) around the remaining part of $A\beta_{42}$ oligomer to interfere its dissociation, then resulting in the higher activation barriers of the PMFs.

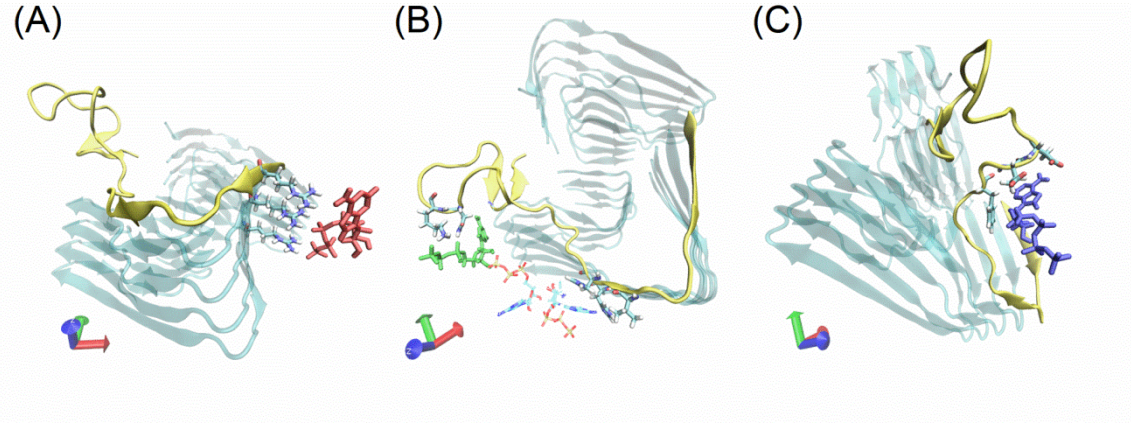

Figure 10. Representative illustration for classification of ATP making contact with dissociated monomer, $A\beta_{42}$(F). (A) ATP making contacts with the remaining part of the $A\beta_{42}$ nonamer simultaneously (red stick). (B) ATPs making other ATPs forming cluster with the remaining part of $A\beta_{42}$ nonamer (green stick). (C) ATPs making no contact with $A\beta_{42}$ nonamer except for $A\beta_{42}$(F) (blue stick). In panel B, ATP cluster is shown by lines. $A\beta_{42}$(F) is highlighted by yellow.

Then, to verify the speculation, we analyzed ATP contact with backbone atoms (N, C and O) of $A\beta_{42}$(F) (*see* Figure S9 in Supporting Information). Assuming convergence of values after 20 ns, we analyzed the values of contacts for the time domain between 20 and 40 ns. 2.4 ± 0.5 ATPs make contact with backbone atoms (N, C and O) of $A\beta_{42}$(F),

and 4.6 ± 0.8 amino acid residues in $A\beta_{42}$(F) make contact with ATPs on their backbone atoms. This observation shows that ATPs steadily make contact with $A\beta_{42}$(F) on the backbone atoms, thus verifying the speculation above. Such ATP contacts are supposed to interfere with rebinding of the dissociated $A\beta_{42}$ monomer to the $A\beta_{42}$ oligomer. As referred above, the role of ATP might be similar to that of morin in the point that it inhibits fibril elongation by blocking the monomer binding on the $A\beta_{42}$ fibril axis end[27,28].

To obtain further insights into ATP contact with the dissociated $A\beta_{42}$ monomer, we examined $A\beta_{42}$(F) backbone-ATP contact by distinguishing ATP parts (hydrophilic tri-phosphate and hydrophobic adenosine). Assuming convergence of values after 20 ns, we analyzed the values of contacts for the time domain between 20 and 40 ns (*see* Figure S10). 0.8 ± 0.2 and 4.2 ± 0.9 backbone atoms make contact with the hydrophilic tri-phosphate and hydrophobic adenosine, respectively. The relatively large number of contact with adenosine could be due to the presence of amino group of adenine and hydroxyl group of ribose. This observation suggests that the hydrophobic part of ATP mainly contributes to contact with the backbone atoms of dissociated $A\beta_{42}$ monomer.

In summary, we could suppose that ATP thus shows the two opposite effects on the $A\beta_{42}$ monomer dissociation process: ATPs suppress monomer dissociation while they prevent refolding of dissociated monomer into oligomer. It is of note that ATP forming

aggregates with $A\beta_{42}$ oligomer make contact with dissociated $A\beta_{42}$ monomer on their backbone atoms. Such an aggregate formation could prevent $A\beta_{42}$ oligomer from recovering on-pathway species. We then suppose that the presence of ATP changes the thermal equilibrium of $A\beta_{42}$ oligomer system from on-pathway species rich one to off-pathway species rich one. Increasing off-pathway species could practically shift thermal equilibrium of $A\beta_{42}$ fibril formation toward that of dissolution. This observation supports our second conjecture that ATP converts $A\beta_{42}$ oligomers into off-pathway species.

We have here proposed the conjecture which reasonably explains the role of ATP, yet it is of note that evidences we have obtained still are not sufficient to verify our conjecture. Actually our present study has not directly examined effects of ATP on unfolded $A\beta_{42}$ monomer association with an oligomer or those on conversion of $A\beta_{42}$ oligomer into off-pathway species. Then these important problems will be investigated in our future research.

Concluding Remarks

We analyzed influences of ATP on an $A\beta_{42}$ oligomer model to examine our two conjectures, 'ATP accelerates the decomposition of $A\beta_{42}$ oligomers into elementary $A\beta_{42}$ components' and 'ATP converts $A\beta_{42}$ oligomers into off-pathway species'.

Recalling destabilization effects of salt on biomolecule complex formation[34,35], the first conjecture seems to be obvious and likely, but we could not obtain any evidences supporting this conjecture. Interestingly, the PMF analyses show that ATP does not accelerate either monomer or protomer dissociation processes and even suppresses $A\beta_{42}$ monomer dissociation. This observation suggests that ATP in aqueous solution does not have positive effects on decomposition of $A\beta_{42}$ oligomer.

By analyzing ATP contact with $A\beta_{42}$ monomer at the fibril axis ends and dissociated $A\beta_{42}$ monomer, we obtained such an insight that ATP contact with backbone atoms of $A\beta_{42}$ monomer is a critical microscopic process to understand the mechanism of $A\beta_{42}$ fibril dissolution under the presence of ATP. The insight supports our second conjecture, conversion of $A\beta_{42}$ oligomer into off-pathway species by ATP. We then consider that ATP dissolves $A\beta_{42}$ fibril by shifting thermal equilibrium of $A\beta_{42}$ oligomer system from on-pathway species rich equilibrium to off-pathway species rich equilibrium. Nevertheless, evidences obtained from the present study still are not sufficient to verify this conjecture so that we will perform additional molecular dynamics simulations for its verification in our future studies.

The molecular diversity of $A\beta_{42}$ fibril structure is widely known[36, 37]. However, the mechanism we proposed here would be applied with no regard to the structural

polymorphism of $A\beta_{42}$ fibril, because it is essentially attributed to ATP contact with the backbone atoms in $A\beta_{42}$ monomers and oligomers. Furthermore, recalling that $A\beta_{42}$ monomer is an intrinsic disorder protein[38], a similar mechanism might hold for ubiquitous dissolution of protein aggregates consisting of other intrinsic disorder proteins such as FUS family proteins[39].

Supporting Information

The Supporting Information is available free of charge on the ACS Publications website. Detailed procedures for unbiased MD, SMD and USMD simulations, Figures and Tables for analyses of these simulations.

Acknowledgements

This work was supported by a Grant-Aid for Scientific Research on Innovative Areas "Chemistry for Multimolecular Crowding Biosystems" (JSPS KAKENHI Grand No. JP17H06351).

Reference

1. Chiti, F.; Dobson, C. M. Protein Misfolding, Amyloid Formation, and Human

Disease: A Summary of Progress Over the Last Decade. *Annu. Rev. Biochem.* **2017**, *86*, 27-68.

2. Miyoshi, N.; Oubrahim, H.; Chock, P. B.; Stadtman, E. R. Age-dependent Cell Death and the Role of ATP in Hydrogen Peroxide-induced Apoptosis and Necrosis. *P. Natl. Acad. Sci. USA* **2006**, *103*, 1727-1731

3. Shigenaga, M. K.; Hagen, T. M.; Ames, B. N. Oxidative Damage and Mitochondrial Decay in Aging. *P. Natl. Acad. Sci. USA* **1994**, *91*, 10771-10778.

4. Ilie, I. M.; Caflisch, A. Simulation Studies of Amyloidogenic Polypeptides and Their Aggregates. *Chem. Rev.* **2019,** *119*, 6956-6993.

5. Lee, J.; Culyba, E. K.; Powers, E. T.; Kelly, J. W. Amyloid-β Forms Fibrils by Nucleated Conformational Conversion of Oligomers. *Nat. Chem. Biol.* **2011,** *7*, 602-609.

6. Patel, A.; Malinovska, L.; Saha, S.; Wang, J.; Alberti, S.; Krishnan, Y.; Hyman, A. A. ATP as a Biological Hydrotrope. *Science* **2017**, *356*, 753-756.

7. Hayes, M. H.; Peuchen, E. H.; Dovichi, N. J.; Weeks, D. L. Dual Roles for ATP in the Regulation of Phase Separated protein Aggregates in Xenopus Oocyte Nucleoli. *Elife* **2018,** *7*, e35224.

8. Hard, T. Protein Engineering to Stabilize Soluble Amyloid β-protein Aggregates for Structural and Functional Studies. *Febs J.* **2011**, *278*, 3884-3892.

9. Gremer, L.; Scholzel, D.; Schenk, C.; Reinartz, E.; Labahn, J.; Ravelli, R. B. G.; Tusche, M.; Lopez-Iglesias, C.; Hoyer, W.; Heise, H. et al. Fibril Structure of Amyloid-β(1-42) by Cryo-electron Microscopy. *Science* **2017**, *358*, 116-119.

10. Wolff, M.; Zhang-Haagen, B.; Decker, C.; Barz, B.; Schneider, M.; Biehl, R.; Radulescu, A.; Strodel, B.; Willbold, D.; Nagel-Steger, L. Aβ42 Pentamers/hexamers Are the Smallest Detectable Oligomers in Solution. *Sci. Rep.* **2017**, *7,* 2493.

11. Maier, J. A.; Martinez, C.; Kasavajhala, K.; Wickstrom, L.; Hauser, K. E.; Simmerling, C. ff14SB: Improving the Accuracy of Protein Side Chain and Backbone Parameters from ff99SB. *J. Chem. Theory. Comput.* **2015**, *11*, 3696-3713.

12. Jorgensen, W. L.; Chandrasekhar, J.; Madura, J. D.; Impey, R. W.; Klein, M. L. Comparison of Simple Potential Functions fro Simulating Liquid Water. *J. Chem. Phys.* **1983**, *79*, 926-935.

13. Kusalik, P. G.; Svishchev, I. M. The Spatial Structure in Liquid Water. *Science* **1994**, *265*, 1219-1221.

14. Joung, I. S.; Cheatham, T. E. Molecular Dynamics Simulations of the Dynamic and Energetic Properties of Alkali and Halide Ions Using Water-Model-Specific Ion Parameters. *J. Phys. Chem. B* **2009**, *113*, 13279-13290.

15. Joung, I. S.; Cheatham, T. E. Determination of Alkali and Halide Monovalent

Ion Parameters for Use in Explicitly Solvated Biomolecular Simulations. *J. Phys. Chem. B* **2008**, *112*, 9020-9041.

16. Meagher, K. L.; Redman, L. T.; Carlson, H. A. Development of Polyphosphate Parameters for Use with the AMBER Force Field. *J. Comput. Chem.* **2003**, *24*, 1016-1025.

17. Bradbrook, G. M.; Gleichmann, T.; Harrop, S. J.; Habash, J.; Raftery, J.; Kalb, J.; Yariv, J.; Hillier, I. H.; Helliwell, J. R. X-ray and Molecular Dynamics Studies of Concanavalin-A Glucoside and Mannoside Complexes - Relating Structure to Thermodynamics of Binding. *J. Chem. Soc. Faraday T.* **1998**, *94*, 1603-1611.

18. Alberty, R. A.; Goldberg, R. N. Standard Thermodynamic Formation Properties for the Adenosine 5'-Triphosphate Series. *Biochemistry* **1992**, *31*, 10610-10615.

19. Case, D. A.; Cerutti, D. S.; Cheatham, T. E., III; Darden, T. A.; Duke, R. E.; Giese, T. J.; Gohlke, H.; Goetz, A. W.; Greene, D.; Homeyer, N. et al. *Amber 17*; University of California: San Francisco, CA, 2017.

20. Le Grand, S.; Gotz, A. W.; Walker, R. C. SPFP: Speed without Compromise-A Mixed Precision Model for GPU Accelerated Molecular Dynamics Simulations. *Comput. Phys. Commun.* **2013**, *184*, 374-380.

21. Berendsen, H. J. C.; Postma, J. P. M.; Vangunsteren, W. F.; Dinola, A.; Haak, J. R. Molecular-Dynamics with Coupling to an External Bath. *J. Chem. Phys.* **1984**, *81*,

3684-3690.

22. Hubbard, S. J.; Thornton, J. M. *NACCESS, version 2.1.1*; Department of Biochemistry and Molecular Biology: University College London, 1993

23. Grossfield, A. *WHAM: The Weighted Histogram Analysis Method, version 2.0.9*; University of Rochester Medical Center: Rochester, NY, 2013.

24. Kumar, S.; Bouzida, D.; Swendsen, R. H.; Kollman, P. A.; Rosenberg, J. M. The Weighted Histogram Analysis Method for Free-Energy Calculations on Biomolecules .1. The Method. *J. Comput. Chem.* **1992**, *13*, 1011-1021.

25. Hub, J. S.; de Groot, B. L.; van der Spoel, D. g_wham-A Free Weighted Histogram Analysis Implementation Including Robust Error and Autocorrelation Estimates. *J. Chem. Theory Comput.* **2010**, *6*, 3713-3720.

26. Humphrey, W.; Dalke, A.; Schulten, K. VMD: Visual Molecular Dynamics. *J. Mol. Graphics & Modelling* **1996**, *14*, 33-38.

27. Ono, K.; Yoshiike, Y.; Takashima, A.; Hasegawa, K.; Naiki, H.; Yamada, M. Potent Anti-amyloidogenic and Fibril-destabilizing Effects of Polyphenols *in Vitro*: Implications for the Prevention and Therapeutics of Alzheimer's Disease. *J. Neurochem.* **2003**, *87*, 172-181.

28. Lemkul, J. A.; Bevan, D. R. Destabilizing Alzheimer's $A\beta_{42}$ Protofibrils with

Morin: Mechanistic Insights from Molecular Dynamics Simulations. *Biochemistry* **2010,** *49*, 3935-3946.

29. Carballo-Pacheco, M.; Strodel, B. Advances in the Simulation of Protein Aggregation at the Atomistic Scale. *J. Phys. Chem. B* **2016,** *120*, 2991-2999.

30. Barducci, A.; Bonomi, M.; Prakash, M. K.; Parrinello, M. Free-energy Landscape of Protein Oligomerization from Atomistic Simulations. *P. Natl. Acad. Sci. USA* **2013**, *110*, E4708-E4713.

31. Cossio-Perez, R.; Pierdominici-Sottile, G.; Sobrado, P.; Palma, J. Molecular Dynamics Simulations of Substrate Release from Trypanosoma cruzi UDP-Galactopyranose Mutase. *J. Chem. Inf. Model.* **2019**, *59*, 809-817.

32. Tran, D. P.; Kitao, A. Dissociation Process of a MDM2/p53 Complex Investigated by Parallel Cascade Selection Molecular Dynamics and the Markov State Model. *J. Phys. Chem. B* **2019**, *123*, 2469-2478.

33. Zhang, L. Q.; Borthakur, S.; Buck, M. Dissociation of a Dynamic Protein Complex Studied by All-Atom Molecular Simulations. *Biophys. J.* **2016**, *110*, 877-886.

34. Gabdoulline, R. R.; Wade, R. C. Simulation of the Diffusional Association of Barnase and Barstar. *Biophys. J.* **1997**, *72*, 1917-1929.

35. Meulen, K. A. V.; Saecker, R. M.; Record, M. T. Formation of a Wrapped DNA-

Protein Interface: Experimental Characterization and Analysis of the Large Contributions of Ions and Water to the Thermodynamics of Binding IHF to H ' DNA. *J. Mol. Biol.* **2008**, *377*, 9-27.

36. Lu, J. X.; Qiang, W.; Yau, W. M.; Schwieters, C. D.; Meredith, S. C.; Tycko, R. Molecular Structure of β-Amyloid Fibrils in Alzheimer's Disease Brain Tissue. *Cell* **2013**, *154*, 1257-1268.

37. Paravastu, A. K.; Leapman, R. D.; Yau, W. M.; Tycko, R. Molecular Structural Basis for Polymorphism in Alzheimer's β-amyloid Fibrils. *P. Natl. Acad. Sci. USA* **2008**, *105*, 18349-18354.

38. Meng, F. J.; Bellaiche, M. M. J.; Kim, J. Y.; Zerze, G. H.; Best, R. B.; Chung, H. S. Highly Disordered Amyloid-β Monomer Probed by Single-Molecule FRET and MD Simulation. *Biophys. J.* **2018**, *114*, 870-884.

39. Wang, J.; Choi, J. M.; Holehouse, A. S.; Lee, H. O.; Zhang, X. J.; Jahnel, M.; Maharana, S.; Lemaitre, R.; Pozniakovsky, A.; Drechsel, D. et al. A Molecular Grammar Governing the Driving Forces for Phase Separation of Prion-like RNA Binding Proteins. *Cell* **2018**, *174*, 688-699.

TOC Graphic